CHALMERS

E_x ^{22}Mg

Data analysis of resonant proton scattering of ^{21}Na in inverse kinematics

Thesis for the degree Master of Science in Fundamental Physics

Fredrik Strannerdahl

Department of Fundamental Physics
Chalmers University of Technology
Gothenburg, Sweden 2013

Data analysis of resonant proton scattering of ^{21}Na in inverse kinematics

Thesis for the degree Master of Science in Fundamental Physics

Fredrik Strannerdahl

Department of Fundamental Physics
Chalmers University of Technology
Gothenburg, Sweden 2013

Abstract

This thesis aims to study a resonant proton scattering experiment performed at CERN-ISOLDE, Geneva, during the summer of 2012. The main focus is detector calibration, data analysis and interpretation of the experimental data.

A radioactive beam of ^{21}Na at 3 MeV/u was impinging on a 5.6 mg/cm^2 polyethylene, $(CH_2)_n$, target in vacuum. Ejectile protons from nuclear reactions of the beam and the target were analyzed by two silicon strip detectors used in a telescope configuration. The resonant elastic scattering reaction ^{21}Na(p,p)^{21}Na is of particular interest due to the importance of ^{22}Mg in stellar nucleosynthesis. Several previously known excited states of ^{22}Mg have been identified at somewhat higher energies than previously reported. Also some, possibly new, states have been observed.

Contents

1 Introduction

Nuclear physics studies the interactions between nucleons which typically takes place at the femtometer, 10^{-15}m, length scale. At these distances the atomic constituents interact via the electromagnetic force, the strong, and the weak force. The strong force holds quarks together to form hadrons as well as keeping protons and neutrons bound in a nucleus. The weak force governs β and particle decays while the electromagnetic force holds atoms together and counteracts the strong force in the nucleus.

A chemical element is defined by the number of protons, Z, in its nucleus. A bound nucleus, X, is in general written as $^A_Z X_N$ or only as $^A X$, where N is the number of neutrons, and $A = Z + N$, the number of nucleons. Different numbers of neutrons in the nucleus give rise to different isotopes and if the number of electrons differs from the number of protons the resulting charged atom is called an ion.

The number of protons and neutrons in the nucleus is important for binding the nucleus together. The binding energy of a nucleus, $^A X$, is defined by the mass difference between the nucleus and its constituents,

$$E_b = (Z m_p + N m_n - m_{^A X}) c^2 \tag{1.1}$$

A positive value of E_b indicates a bound nucleus.

In a similar manner is the *Q-value* of a reaction defined as

$$Q = E_{b_{final}} - E_{b_{initial}} = (m_{initial} - m_{final}) c^2 \tag{1.2}$$

A value of $Q > 0$ gives an *exothermic* reaction, and a net energy is produced by the reaction. The opposite, $Q < 0$, is said to be *endothermic*, and an energy equal to Q has to be provided to make the reaction possible.

Unstable nuclei disintegrate after a certain time via radioactive decay, and finally end up as stable ones which do not decay any further. In the chart of nuclides, stable nuclei usually have their proton rich isotopes to the left and the neutron rich to the right giving rise to a band of stable nuclei, *the valley of stability*. Far from this valley the proton, or neutron, can no longer be bound to the nucleus. These are the *proton drip line* and the *neutron drip line*, nuclei close to either one of them are called *exotic nuclei*.

Facilities, such as CERN-ISOLDE, which are able to produce radioactive exotic ions make it possible to study nuclei close to the drip lines.

1.1 Purpose

The purpose of this thesis is to analyze data from a resonant proton scattering experiment, IS512, performed during the summer of 2012 at CERN-ISOLDE. The main focus is on detector calibration and the analysis of ^{21}Na+p scattering data. From the spectrum of scattered protons it might be possible to identify excited states in ^{22}Mg.

2 Theory

2.1 Interaction of radiation with matter

When charged particles interact with a detector, or matter in general, they transfer some or all of their energy to the detecting material. The energy loss for heavy charged particles[1] is mainly due to Coulomb scattering of the atomic electrons. The amount of energy lost per unit length in the interaction is described by the *Bethe-Bloch formula*, Ref. [12], Eq. (2.1)

$$\frac{\mathrm{d}E}{\mathrm{d}x} = \left(\frac{e^2}{4\pi\epsilon_0}\right)^2 \frac{4\pi z^2 N_0 Z \rho}{mc^2\beta^2 A} \left[\ln\left(\frac{2mc^2\beta^2}{I}\right) - \ln(1-\beta^2) - \beta^2\right] \qquad (2.1)$$

N_0 is Avogadro's number, m is the electron mass, $\nu = \beta c$ is the velocity of the incoming particle and ze its charge. Z, A and ρ are the atomic number, atomic weight and the density of the absorbing material, respectively. The mean excitation energy of the atomic electrons is represented by I.

Some important characteristics of Eq. (2.1) can be stressed here. For particles interacting with the same material the energy is only a function of the charge, mass and velocity of the particle. Further, if the logarithmic variation due to the velocity is small over the actual range, which often is the case, Ref. [16], Eq. (2.1) can be simplified and used for particle identification according to

$$E\frac{\mathrm{d}E}{\mathrm{d}x} \propto M z^2 \qquad (2.2)$$

where M is the mass of the incoming particle and z its charge in units of e.

The penetration depth of a incoming particle, referred to as *range*, can be calculated by Equation (2.3)

$$R = \int_T^0 \left(-\frac{\mathrm{d}E}{\mathrm{d}x}\right)^{-1} dE \qquad (2.3)$$

The range of protons and α particles was calculated using the SRIM software, Ref. [8], and can be seen for energies between 0 and 12 MeV in Figure 2.1. These range tables can be used to calculate the energy loss.

2.2 Resonant scattering

Typical binary nuclear reactions are written as

---

[1]Particles heavier than the electron are considered heavy. For electrons and positrons some corrections have to be made to the Bethe-Bloch formula.
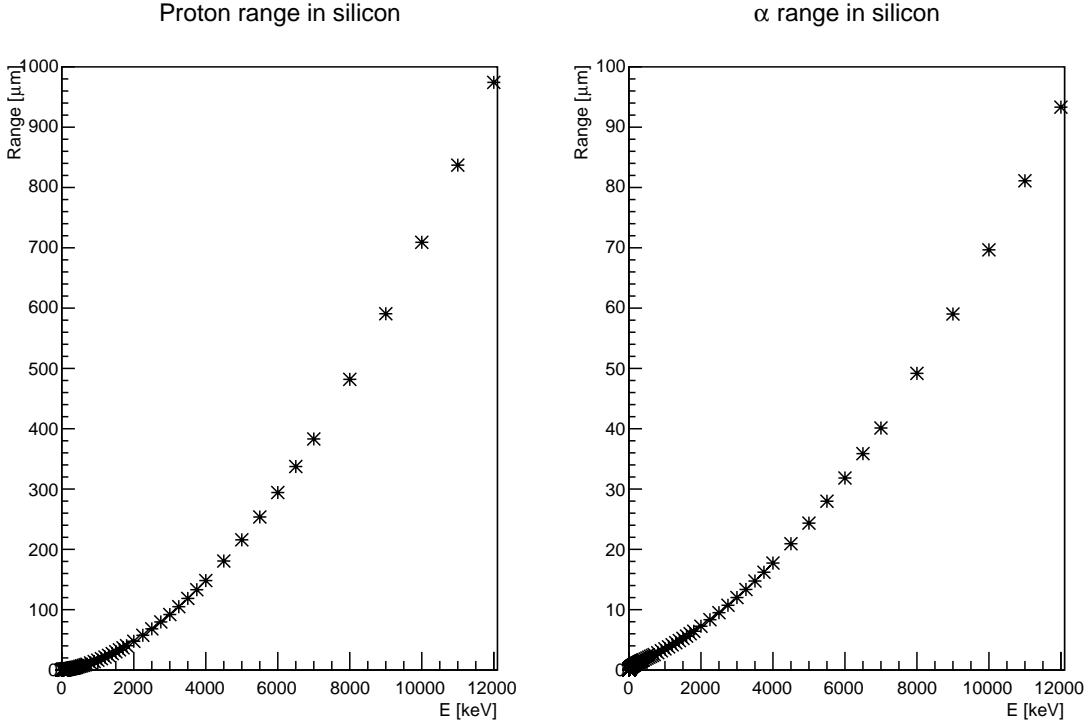
Figure 2.1: Penetration depth as a function of energy for protons and α particles in silicon calculated by SRIM.

$$a + X \; \rightarrow \; Y + b \qquad \text{or} \qquad X(a,b)Y$$

where a is the projectile, X the usually stationary target, Y is the heavier reaction product and b the lighter ejectile which is often the one that is detected and measured. If both the incoming and outgoing particles are the same the reaction is referred to as a *scattering* process. If the reaction products are in the ground state interaction the process is called *elastic scattering*, and *inelastic scattering* if Y is in an excited state.

One possibility for nuclear reactions to proceed, if the impact parameter is small, is by forming a quasibound intermediate state called a *compound nucleus*. The reaction then takes the form of a two step process, the formation of a compound nucleus and the subsequent decay.

$$a + X \; \rightarrow \; C^* \rightarrow \; Y + b \qquad\qquad (2.4)$$

where C^* indicates the compound nucleus.

Resonant reactions are a type of compound nucleus reactions with discrete energy levels of the intermediate state. These reactions occur only for certain energies of the incoming particle. That is if the center of mass energy of the entrance channel, $E_{cm}+Q$, where $E_{cm} = E_{cm}^X + E_{cm}^a$, happens to match an energy level, E_X, of the excited compound nucleus. Since these reactions only take place at energies $E_{cm} + Q = E_X$ they are referred to as resonant and the compound nucleus sometimes as a resonance.

While compound reactions in general can decay in a variety of ways, independent of the entrance channel, the quasi bound nucleus in resonant reactions have more of a two particle structure. This implies that they usually only have two decay possibilities, by re-ejecting the incoming particle or by γ emission [12].

In the resonant scattering process of ^{21}Na+p, ^{22}Mg is the resonance which quickly decays back to a proton and ^{21}Na in ground state or a low lying excited state [22].

Due to the fact that ^{21}Na is a radioactive isotope with a half-life of about 22.5 s, Ref. [6], it is not very well suited as a reaction target. Thus, using protons as projectiles is not possible but the protons have to be in the reaction target an instead being hit by the radioactive ^{21}Na beam. Such reactions, with heavy projectiles on a lighter target, are called *inverse kinematics* reactions.

2.3 Inverse elastic resonant scattering kinematics

To derive the excitation energy of the compound nucleus momentum conservation of the elastic resonant scattering process is used. For a heavy incoming particle X with energy E on stationary target a one has

$$m_X \mathbf{v} = (m_X + m_a)\mathbf{v_{cm}} \Leftrightarrow \mathbf{v_{cm}} = \frac{m_X}{m_X + m_a}\mathbf{v}, \qquad\qquad (2.5)$$

here, $\mathbf{v_{cm}}$ is the velocity of the center of mass frame and the compound nucleus, $\mathbf{v}$ is the velocity of the incoming particle X in the laboratory and $|\mathbf{v_{cm}}| = v_{cm}$, yielding

$$E_{cm} = \frac{m_X + m_a}{2}(v_{cm})^2 = \frac{m_X}{m_X + m_a}E \tag{2.6}$$

By using (2.5) and the fact that the target is at rest in the laboratory, $|\mathbf{v_{cm}^a}| = v_{cm}$, the center of mass energy of a is

$$E_{cm}^a = \frac{m_a}{2}(v_{cm})^2 = \frac{m_a \cdot m_X}{(m_X + m_a)^2}E \tag{2.7}$$

and for the incoming particle

$$E_{cm}^X = \frac{m_X}{2}(v - v_{cm})^2 = \frac{m_X}{2}\left(\frac{m_a}{m_X + m_a}v\right)^2 = \left(\frac{m_a}{m_X + m_a}\right)^2 E \tag{2.8}$$

The excitation energy, E_X^C, of the compound system can then be calculated as

$$E_X^C = S_a + E_{cm}^a + E_{cm}^X \tag{2.9}$$

where S_a is the particle separation energy and is given by the mass difference

$$S_a = (m_X + m_a - m_C)c^2 \tag{2.10}$$

A sketch of the geometry of the decay of the compound system in the laboratory and center of mass frames can be seen in Figure 2.2.

By again using $v_{cm}^a = v_{cm}$ and the law of cosines on the triangle (ABC) gives

$$(v^a)^2 = 2(v_{cm})^2(1 + \cos(\phi_{cm})) = 2\left(\frac{m_X}{m_X + m_a}v\right)^2(1 + \cos(\phi_{cm})) \tag{2.11}$$

Further, $\phi_{cm} = 2\theta_{lab} \Rightarrow 1 + \cos(\phi_{cm}) = 2\cos^2(\theta_{lab})$, so the energy of the light scattered particle, a, in the lab frame is given by

$$
\begin{aligned}
E^a &= \frac{m_a}{2}(v^a)^2 = 2m_a\left(\frac{m_X}{m_X + m_a}v\right)^2\cos^2(\theta_{lab}) = \frac{4m_a \cdot m_X}{(m_X + m_a)^2}E\cos^2(\theta_{lab}) \\
&\Leftrightarrow E = \frac{E^a(m_X + m_a)^2}{4m_a \cdot m_X\cos^2(\theta_{lab})}
\end{aligned}
\tag{2.12}
$$

Substituting the last expression of Eq. (2.12) into Eq. (2.9) gives

$$E_X^C = S_a + \frac{m_a \cdot m_X}{(m_X + m_a)^2}E + \left(\frac{m_a}{m_X + m_a}\right)^2 E = S_a + \frac{E^a(m_X + m_a)}{4m_X\cos^2(\theta_{lab})} \tag{2.13}$$

So to determine the excitation energies of the decaying system only knowledge about the masses involved and the energy and angle of the light scattered particle is required. Compared to conventional scattering processes in direct kinematics, where the light particle is the projectile, the inverse kinematics method has a gain factor of about 4 for the laboratory energy of the light ejectile at $\theta_{lab} \sim 0°$[13].
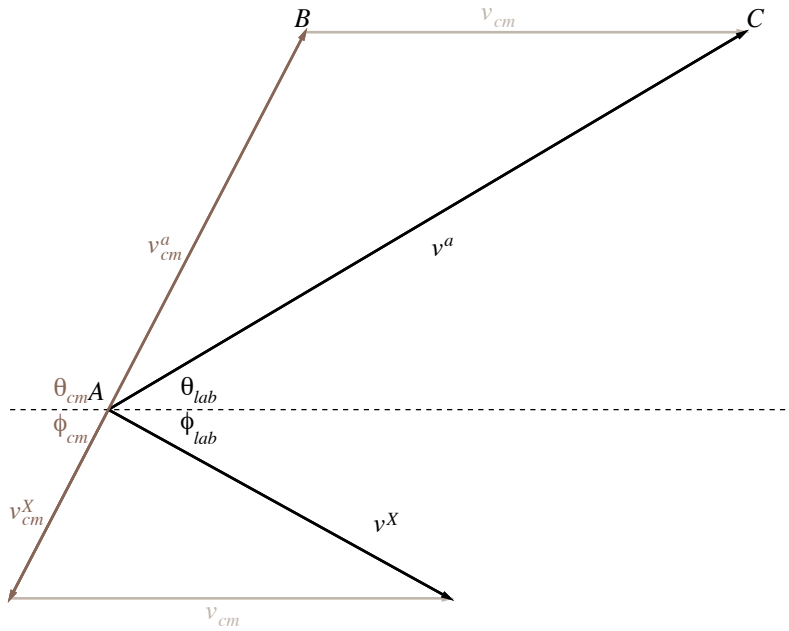
Figure 2.2: Schematic drawing of the decay of the compound nucleus in the laboratory and center of mass frames. Small scattering angles in the laboratory frame correspond to large angles in center of mass via $\theta_{cm} = \pi - 2\theta_{lab}$. All angles are with respect to the dashed line.

Figure 2.3 shows kinetic energies and angles of protons scattered of a ^{21}Na beam at 3 MeV/u[2].

2.4 ^{22}Mg and the hot CNO-cycle

The structure of ^{22}Mg has been studied intensively by both theorists and experimentalists for the last decades. This because of its importance for calculating astrophysical reaction rates of ^{21}Na(p,γ)^{22}Mg[3], and the Hot CNO-cycle breakout reaction ^{18}Na(α,p)^{21}Na proposed by Wiescher *et al.*[14], see Figure 2.4, .

Excited states of ^{22}Mg have previously been studied by a variety of reaction channels such as ^{24}Mg(p,t)^{22}Mg, ^{24}Mg(^{4}He,^{6}He)^{22}Mg, ^{12}C(^{16}O,^{6}He)^{22}Mg but also directly by ^{18}Ne(α,p)^{21}Na and elastic resonant scattering of ^{21}Na+p [19].

---

[2]A "back of the envelope calculation" of Eq. (2.13) using $E_p = 11$ MeV at $\theta_{lab} = 0°$, $m_p = 1u$, $m_{Na} = 21u$, $S_p = 5.5$ MeV gives $E_X^{Mg22} \approx 8.4$ MeV. States above 8.5 MeV, as reported in Ref. [19], will probably not be accessible at current beam energy.

[3]For determining the amount of ^{22}Na produced by ^{21}Na(p,γ)^{22}Mg(β^+)^{22}Na in nova events [15].
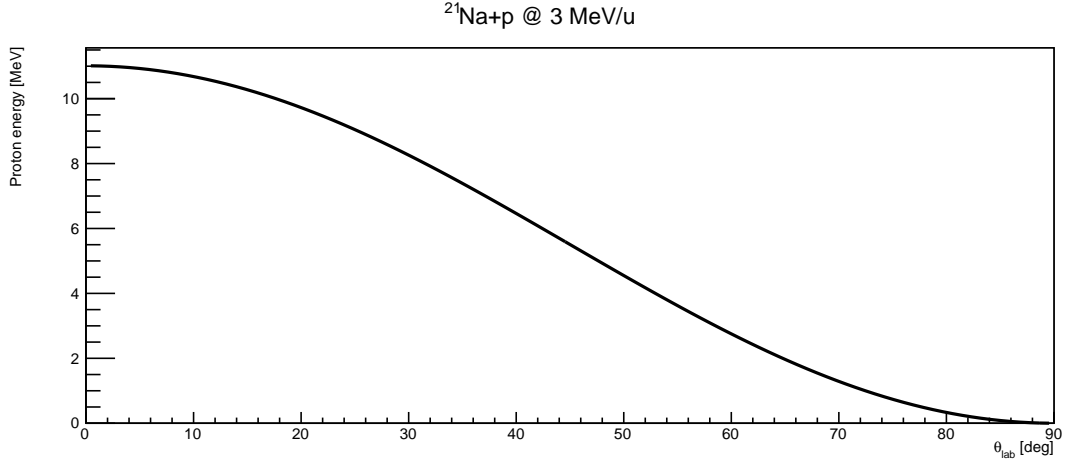
Figure 2.3: Proton energy versus scattering angle, Eq. (2.12), in the laboratory system for resonant elastic scattering of a 3 MeV/u ^{21}Na beam in inverse kinematics. The protons have a maximum energy of about 11 MeV at $\theta_{lab} = 0°$.

The HCNO I cycle determines the nucleosynthesis up to temperatures of T$\lesssim$ 0.4 GK, Ref. [22], in stellar environments. The slowest processes in HCNO I are the β decays ^{14}O$(\beta^+\nu)^{14}$N and ^{15}O$(\beta^+\nu)^{15}$N, these are the waiting points of the nucleosynthesis path. At these temperatures the HCNO I is limited by the drip line isotopes ^{15}F and ^{16}F. When the temperature and density of the star increase the α particle and proton capture processes become faster than the β^+ decays. The HCNO II cycle might then pass ^{15}F and ^{16}F and subsequently break out of the HCNO II cycle via ^{15}O$(\alpha,\gamma)^{19}$Ne to the *rp process*, where heavier elements are produced on the proton rich side of the stability line by consecutive proton capture.

At even higher temperatures, $T \gtrsim 0.8$ GK, the ^{18}Ne$(\alpha,$p$)^{21}$Na breakout becomes available and is thereby able of bypassing the ^{15}O$(\alpha,\gamma)^{19}$Ne path, Figure 2.4.

Since many of these reactions proceed via resonances, Ref. [22], the excited states above the α threshold in ^{22}Mg at 8.142 MeV, Ref. [19], are of particular astrophysical interest due to the ^{18}Ne$(\alpha,$p$)^{21}$Na reaction.
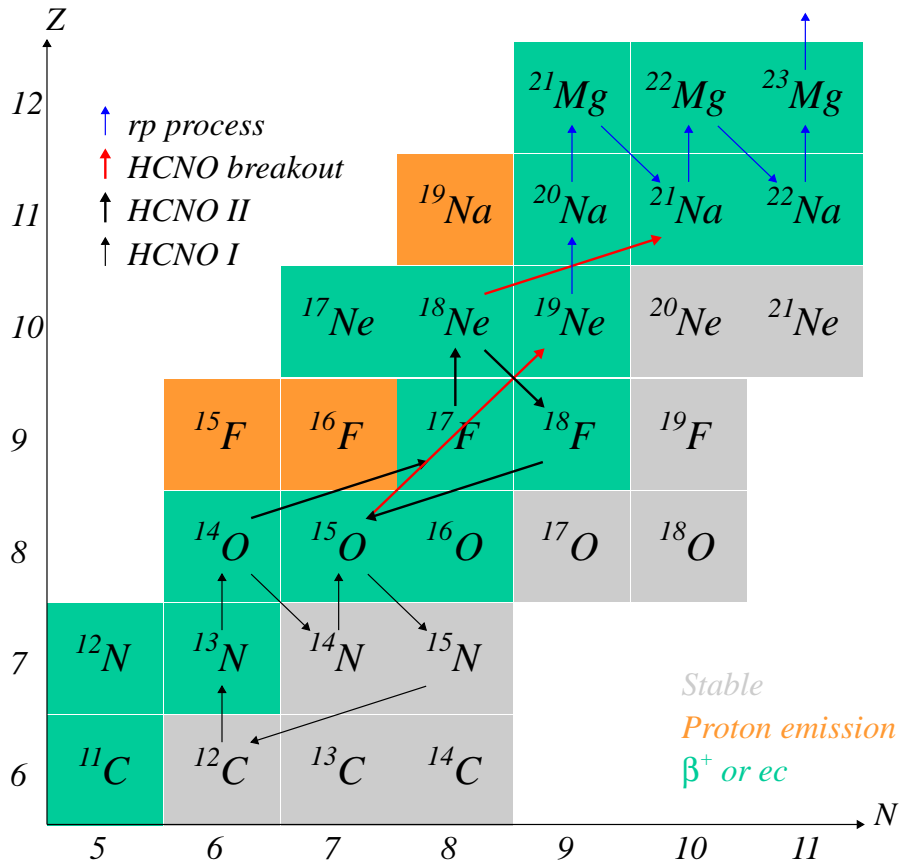
Figure 2.4: Part of the chart of nuclides for the proton rich side of the line of stability with corresponding decay modes. The hot CNO-cycles, the rp-process and possible breakouts are indicated by arrows. The ^{18}Ne(α,p)^{21}Na reaction is thought to proceed via resonances in ^{22}Mg.

3 Detectors

3.1 Semiconductor detectors

Semiconductor materials, most often Si or Ge, can be used to detect nuclear radiation. They provide decent position and energy resolution compared to gas filled and scintillator detectors. The energy resolution of semiconductors are about one order of magnitude larger than that of gas filled detectors and almost two orders of magnitude larger than that of a scintillator detector [9]. Both Ge and Si have four valence electrons and form covalent bonds with four other neighboring Si (or Ge) atoms and thereby getting a filled valence band and an empty conduction band. The energy gap of semiconductor materials is in the order of 1 eV which implies that electrons can be thermally excited from the valence band to the conduction band even at room temperature. Therefore small amounts of dopants with one more or one electron less are added to control the electrical conduction. Adding an atom with 5 valence electrons causes four of them to be part of the covalent bond while the fifth will be able to move through the lattice. These are referred to as *donor states* and are located just below the conduction band and the material is then an *n-type semicondutor*. If instead an atom with 3 valence electrons is added, the absence of one electron - a *hole* - in the covalent bond forms *acceptor states* of a *p-type semiconductor*.

When a p-type and an n-type semiconductor are brought together electrons diffuse to the p-type side and combine with the holes, this creates an insulating *depletion region* without free charge carriers. A reverse bias voltage is then applied to increase the depleted zone and give the the detector its full active volume. When nuclear radiation reaches the depleted region of the detector electron-hole pairs are created. Due to the the high bias voltage these will quickly drift to the p-side (holes) and n-side (electrons). The charge is collected and a pulse which amplitude is proportional to the energy of the impinging particle is formed.

Two Si detectors were used during the IS512 experiment. One *Double Sided Silicon Strip Detector - DSSSD* with read-out strips at both the front and the back side of the detector and another *Single Sided Silicon Strip Detector - SSSSD* with read-out strips only on the front side. Segmented detectors are achieved by implanting thin p-dopes strips on one side of a n-doped Si crystal and heavily doped n^+-strips on the other side. Each strip then works as an individual detector which makes a silicon strip detector position sensitive. By crossing the strips of the front and back side 2D spatial resolution is achieved.

To be able to read out the energy deposited in the detector there is a thin *dead layer* at both sides of the active detector volume where energy is lost but not detected. These losses have to be taken into account when calculating the actual energy of the particle.

3.2 Telescope configuration

Using detectors in a telescope configuration allows to distinguish different particle species from the experimental data. First the particles interact with a thin detector, depositing only a part of their energy. This detector is backed up by a second, and often thicker, detector which usually stops the particle and detects the rest of the total kinetic energy. The energy transferred to each detector is given by the Bethe-Bloch equation, Eq. (2.1). Due to the different thickness of the two detectors and thereby different energy deposition, the first one is referred to as a ΔE-detector and the second one as an E-detector[1]. Due to the fact that the energy loss in the detectors depends only[2] on the total energy, mass and charge of the incoming particles, different particles can be seen as hyperbolas in a plot of ΔE versus E. A simulation with *ggland*[3], based on Geant4[4], of protons, deuterons and α particles can be seen in Figure 3.1. If a particle has high enough energy it can punch though even the second detector and thereby all the energy is not detected. The proton *punch-through* can be seen just above 12 MeV in the E-detector, marked E_{SSSSD} in Figure 3.1.
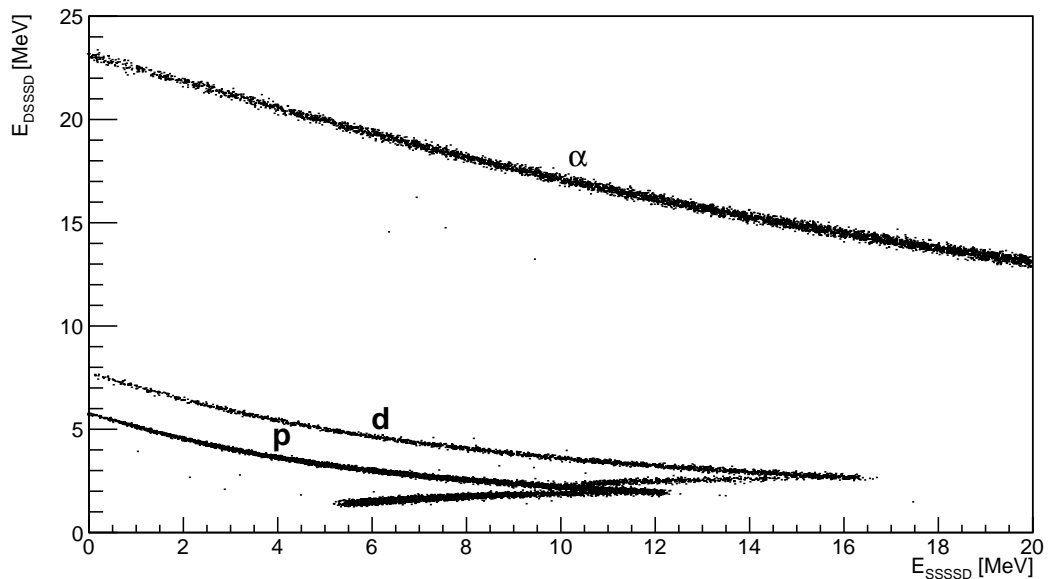
Figure 3.1: Simulation of protons, deuterons, and α particles in a Si ΔE-E telescope. The thickness of the ΔE and E detectors are 300 μm and 1 mm respectively.

---

[1]During the IS512 experiment a DSSSD was used as the ΔE-detector and an SSSSD as the E-detector.
[2]For particles interacting with the same detecting material.
[3]Command line simulation tool by Håkan Johansson [2].
[4]Software for simulating particle interactions with matter [3].

4 Experimental setup

4.1 Beam production
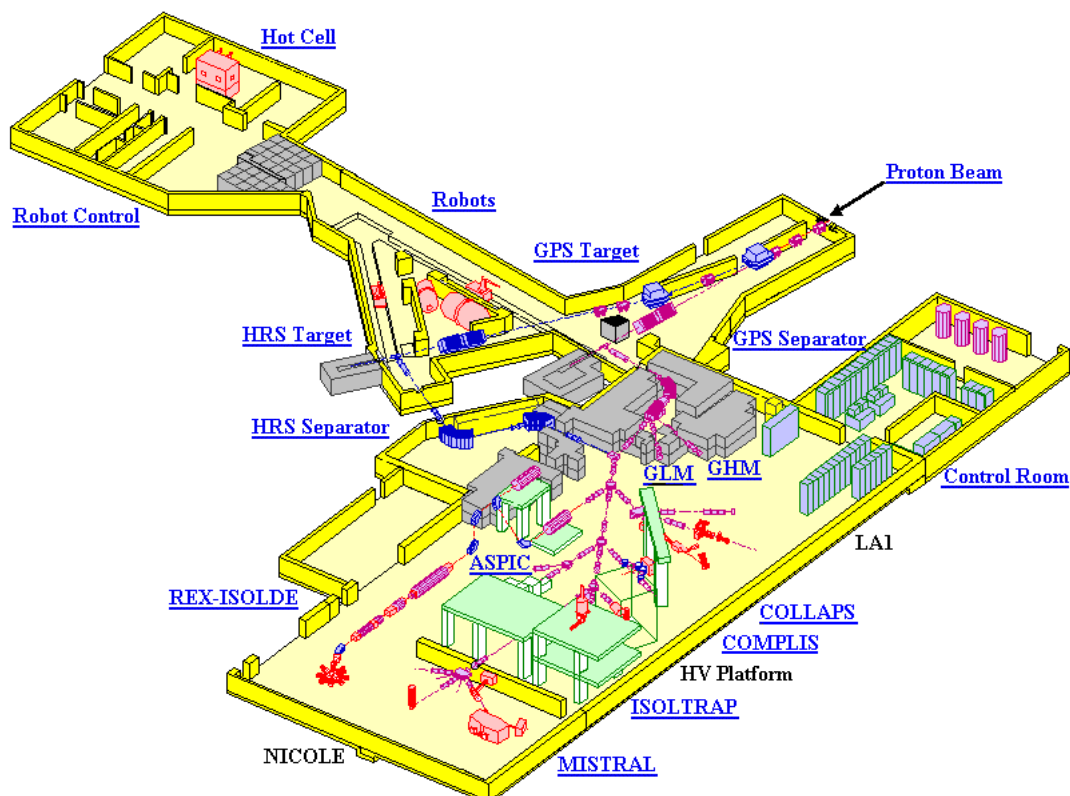
Figure 4.1: Overview of the ISOLDE facility [4].

The creation of a radioactive ion beam at CERN-ISOLDE requires several steps. First, protons are injected from the linear accelerator *Linac2* to *PS Booster*[1] where the protons are accelerated from 50 MeV to ~ 1.4 GeV, Ref. [7], before the proton beam is delivered to ISOLDE, Figure 4.1. Ions are then produced by spallation, fragmentation or fission reactions in a production target at either the *General Purpose Separator, GPS* or the *High Resolution Separator, HRS*. In the case of ^{21}Na production for the

---

[1]Proton Synchrotron Booster.

IS512 experiment a SiC target was used at the HRS. The reaction products that diffuse out of the production target are slightly ionized, 1^+, before they are extracted from the ion source by a 50 kV DC field. The radioactive ions are then sent to an analyzing magnetic separator where different masses are bent according to their charge-to-mass ratio. When the desired radioactive ion beam is selected it leaves ISOLDE at energies of around 50 keV. At REX[2] the beam particles are cooled, charge-bred to a higher charge state, and once again mass separated before reaching a linear accelerator where the particles are accelerated to 3 MeV/u. Finally they are delivered to the experiment.

The ^{21}Na beam impinged on the $(CH_2)_n$ target mounted in a scattering chamber, with a vacuum of about $6 \cdot 10^{-7}$ mbar. The reaction products were scattered into the Si telescope about 223 mm downstream covering angles up to $\theta_{lab} \sim 10°$, where their energy and scattering angle were measured. The active thickness of the DSSSD was 300 μm and that of the SSSSD was 1 mm.
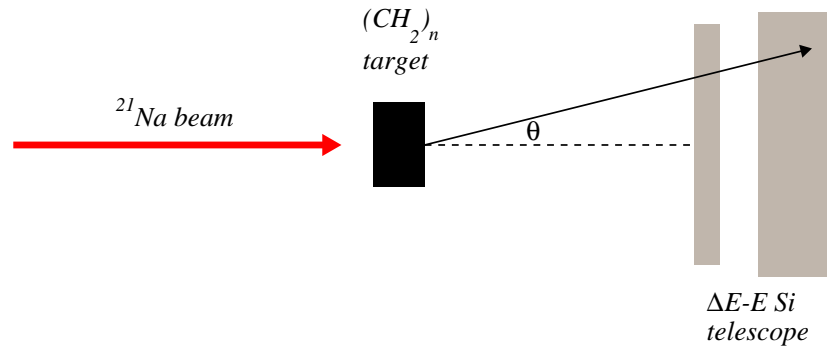
Figure 4.2: Schematic drawing of the IS512 setup.

---

[2]Radioactive beam EXperiment.

5 Calibration

Before the detectors can be used for analyzing the experiment they have to be calibrated. This was done by a quad α-source with known energies, ^{148}Gd, ^{239}Pu, ^{241}Am and ^{244}Cm. All of these, except ^{148}Gd, have two or more major α lines close in energy which could not be distinguished. Therefore weighted mean values for these were used: $E_{Gd} = 3182.690$ keV, $E_{Pu} = 5148.372$ keV, $E_{Am} = 5479.838$ keV and $E_{Cm} = 5795.038$ keV [6]. The dead layers of both the DSSSD and the SSSSD were 2 μm thick[1].

5.1 Data handling

All data from the IS512 experiment was analyzed by the C++-based framework ROOT, Ref. [5], which is developed at CERN and designed for particle physics data analysis.

The mapping from raw data to ROOT-files was done using the software *UCESB - Unpack and Check Every Single Bit*, Ref. [10], by Håkan Johansson, Chalmers. The ROOT-files contains all experimental data and is listed event-by-event and stored in a *Tree*.

The output of each ADC[2] channel is stored as a *Branch* of that Tree. For both the detector calibration and the ^{21}Na+p analysis the data was reconstructed. New Trees were created and additional, calibrated, Branches were added when appropriate.

5.2 DSSSD

Because of high multiplicity[3] of the DSSSD due to low energy thresholds all the calibration data had to be reconstructed before the calibration could be done. By identifying the α peaks in the uncalibrated energy spectra an energy gate could be set at 400 ch $\leq$ E $\leq$ 1200 ch, Figure 5.1. A new Tree was then created and the actual multiplicity was greatly decreased since most of the noise was suppressed, Figure A.2.

The DSSSD used during the experiment had an active area of 58 x 58 mm, consisting of 32 strips on the front side and 32 intersecting strips on the back side, creating 1024 detecting pixels. The probability of hitting a detector pixel located at (x,y) is given by

---

[1]The thickness of the detector dead layer is given as a silicon equivalent distance.
[2]Analog to Digital Converter.
[3]The multiplicity is the number of strips firing during the same event.
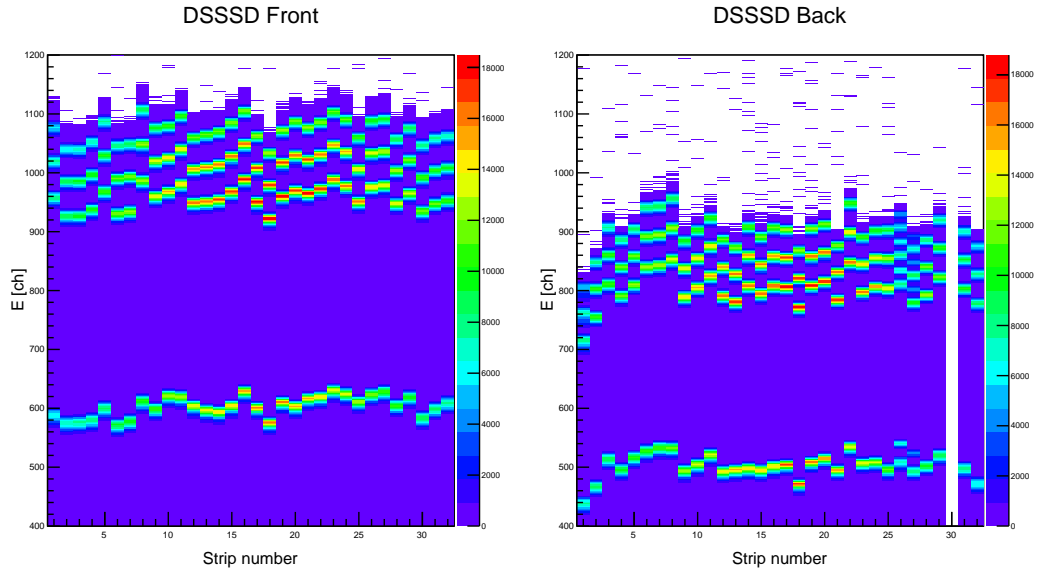
Figure 5.1: Raw α spectra of the DSSSD.

$$P(x,y) = P_0 \frac{\cos^3\left(\tan^{-1}\left(\frac{\sqrt{(x-x_0)^2+(y-y_0)^2}}{d_0}\right)\right)}{d_0^2} \qquad (5.1)$$

where (x_0,y_0) is the closest point of the detector to the source, d_0 is the distance from the source to the closest point of the detector and P_0 is a constant [11]. This probability function could then be fitted to the actual 2D histogram from the calibration run. The measured hit pattern and a corresponding of probability function can be seen in Figure 5.2. Strip 30 of the back side of the DSSSD was not working during the experiment[4].

According to this fit, the alpha source was placed 23.2 strip widths, or 42mm, from the detector and located in front of strip 18 of the back side and strip 16 of the front side.

Due to the short distance between the detector and the source, the α particles had to penetrate a different effective dead layer thickness before reaching the active volume of the detector depending on which pixel was hit. The effective dead layer thickness for each pixel is given by $d/\cos\theta$, where θ is the angle between the shortest distance from the source to the detector and the pixel being hit while d is the dead layer thickness. With this information the effective dead layer thickness for each pixel can be calculated. The energy loss does not only depend on the dead layer thickness

---

[4]Strip 26 and 27 showed double α peaks, and strip 1 seemed to be changing gain factor during the experiment. All these were located on the back side of the detector and were omitted during the analysis.
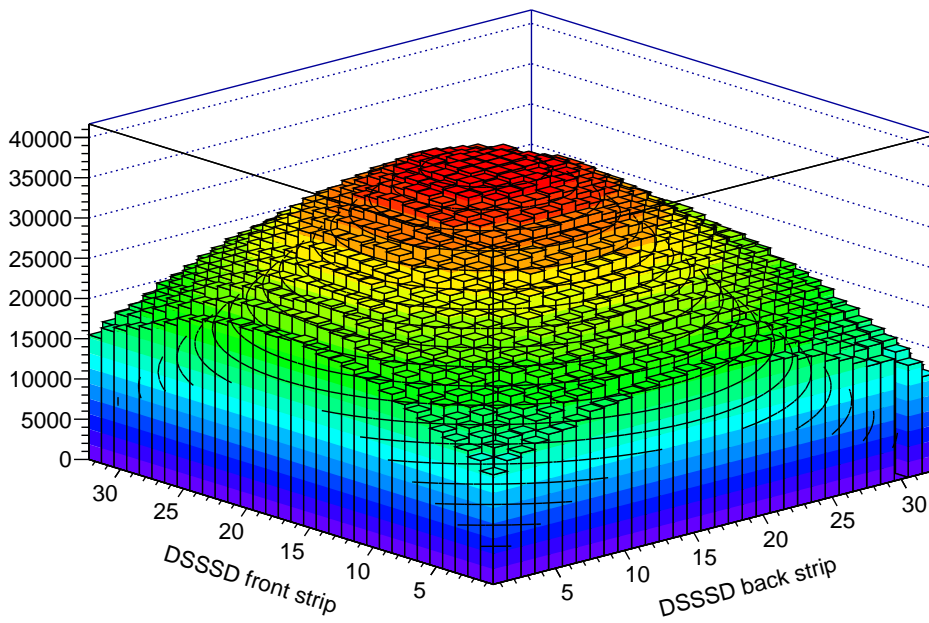
Figure 5.2: Hit pattern from the quad α source calibration with fitted probability function, see Eq. (5.1).
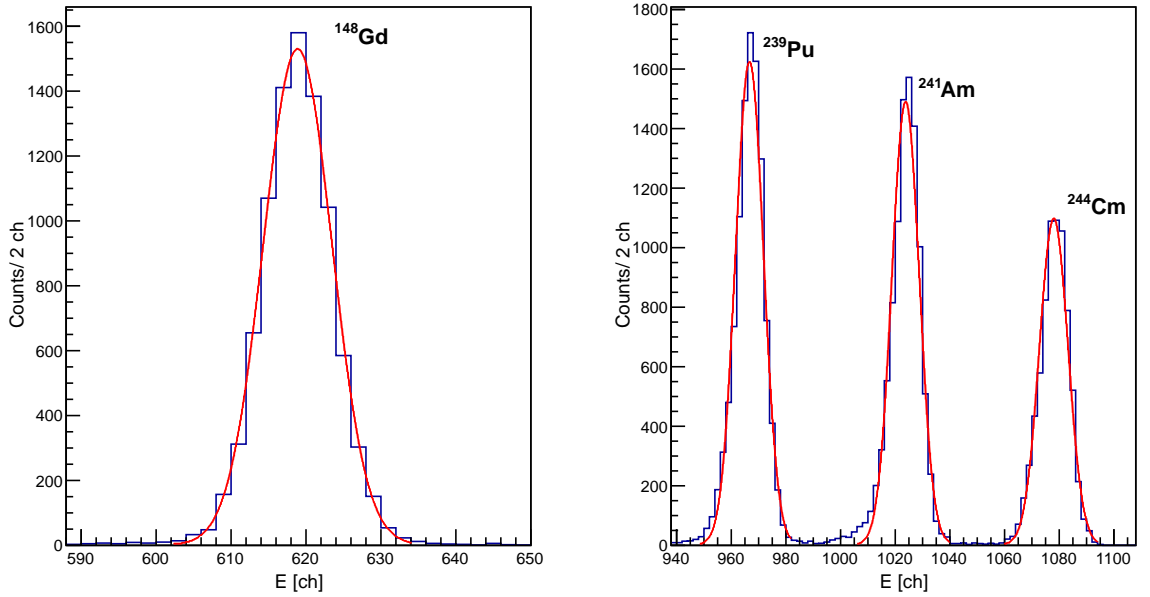
Figure 5.3: Typical α spectrum from the calibration run. This plot shows the uncalibrated energy from the DSSSD at the intersection of front strip 21 and back strip 16 with Gaussian fits. All, except the ^{148}Gd peak, consist of several α peaks so the Gaussian centroid does not necessarily coincide with the maximum count channel.

but also on the energy of the incoming particle. The penetration depth of α particles as a function of their energy is given in Figure 2.1 and the energy loss is calculated according to this graph.

The DSSSD was energy calibrated pixel by pixel by first finding the α peaks of each pixel given in channels, then a Gaussian fit was made for each of them, Figure 5.3. The energy was assumed[5], to be a linear function of channel for every detector pixel (i,j),

$$E_{i,j} = G_{i,j} \cdot (ch+R) + O_{i,j} \tag{5.2}$$

where G represents the gain factor and O the pixel offset, R is a uniformly distributed random number $[-0.5, 0.5)$. $G_{i,j}$ and $O_{i,j}$ was saved as 32x32 matrices for each side of the detector. The mean value of the offset and gain factors for each strip were also calculated and saved for energy matching purposes. The actual deposited energy was then calculated by Eq. (5.2).

---

[5]Detector linearity checked during experiment [18].
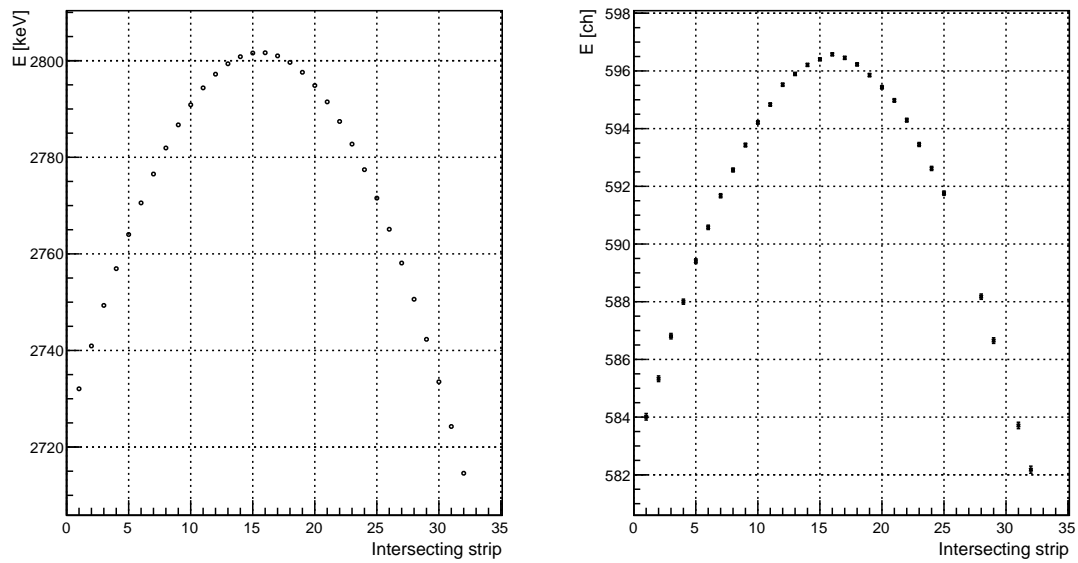
Figure 5.4: ^{148}Gd peaks originating from 3182.690 keV α particles in strip 8 on the front side of the DSSSD with intersecting strips on the x-axis. To the left: the energy that reaches the active volume of the detector after the dead layer calculated by SRIM. To the right: the actual measured energy, in channels, from the calibration run.
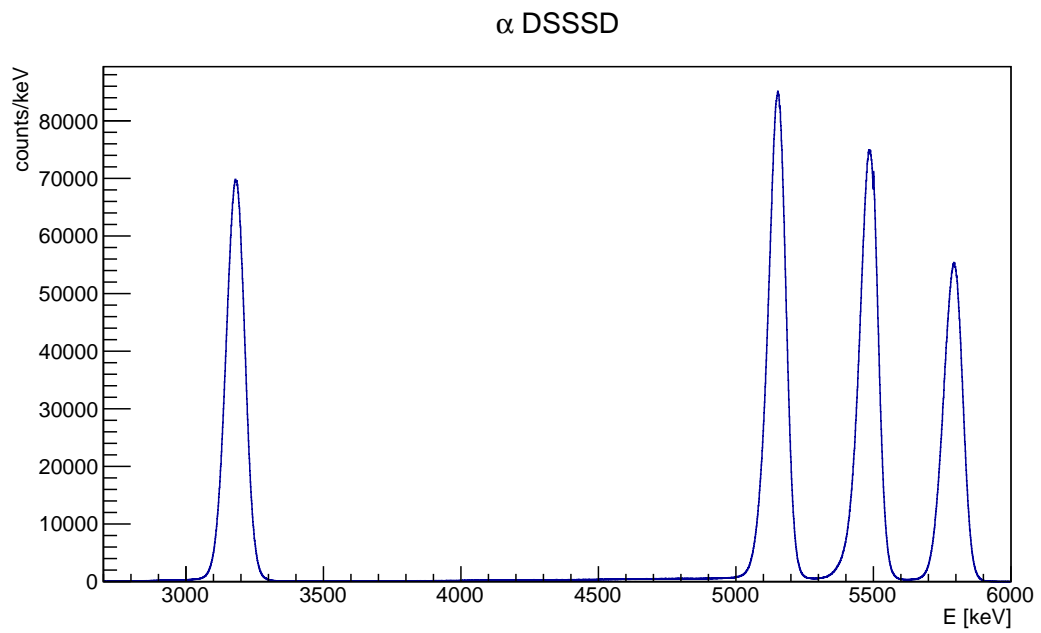
Figure 5.5: The figure presents a calibrated α spectrum as a projection of all the p-side pixels of the DSSSD. The resolution, FWHM, is about 80 keV in the lab and $\sim$ 20 keV in the center of mass system.

5.3 SSSSD

A similar method was used for the calibration of the 62 x 62 mm E-detector, the difference is that the SSSSD used in this experiment is position-sensitive in only one spatial direction - in this case the y-direction. This means that it is not possible to determine where in the strip a particle actually hits. Therefore a weighted mean value for the dead layer thickness of each strip had to be used for the calibration. Again using Eq. (5.1) to find the probability of hitting a certain detector position[6], an effective mean thickness, d_j, of each strip was calculated by

$$d_j = \frac{\sum_{i=1}^{32} P_{ij} \cdot d_{ij}}{\sum_{i=1}^{32} P_{ij}} \tag{5.3}$$

where d_{ij} is the effective dead layer thickness of pixel (i,j) and P_{ij} the probability of hitting that specific pixel given by Eq. (5.1). Due to low statistics of the calibration data for the SSSSD a the exact source position in the x-direction could not be calculated, so the source was assumed[7] to be located at a central position - 16 strip widths from the edge - of the detector in this direction. A fit could then be made to the hit pattern, Figure 5.6, by calculating the probability of hitting a specific strip y,

$$P(y) = P_0 \sum_{i=1}^{32} \left(\frac{\cos^3 \left(\tan^{-1} \left(\frac{\sqrt{(i-0.5-16)^2 + (y-y_0)^2}}{d_0} \right) \right)}{d_0^2} \right), \tag{5.4}$$

resulting in a distance between the source and the target of about 27 strip widths or 53 mm in front of strip 17. The SSSSD hit pattern can be seen in Figure 5.6 together with a fit of Eq. (5.4) and a *ggland* simulation where a central x-position was assumed, $y_0 \approx 17$, $d_0 \approx 27$ strip widths are taken from the fit. The energy resolution of the SSSSD was about 95 keV in the laboratory frame or 24 keV in center of mass. The total resolution[8] of the the telescope system is approximately 31 keV in the in the center of mass system.

A linear fit, according to Eq. (5.5), was then made for each strip. Plots and fitting parameters are presented in Figure A.5.

$$E = G \cdot (ch + R) + O \tag{5.5}$$

Again G is the gain factor, O the offset and R a uniformly distributed random number $[-0.5, 0.5)$.

---

[6]Each strip was considered to be built up of 32 pixels and thereby Eq. (5.1) could be used again.

[7]A central source position ± 4 strip widths gives an energy loss difference ≤ 4 keV due to the effective dead layer thickness.

[8]Assuming the individual resolutions are uncorrelated.
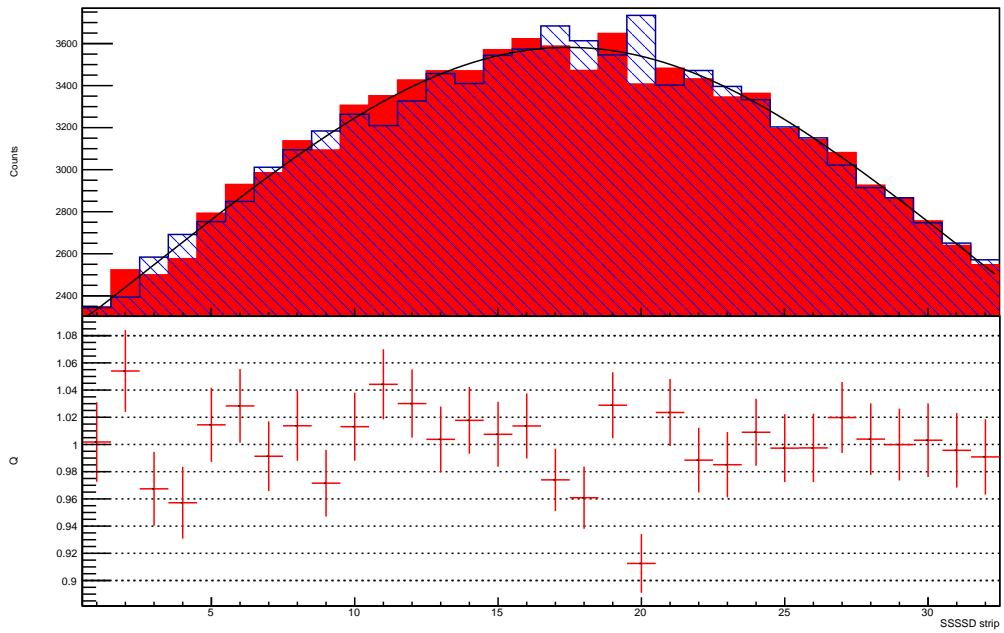
Figure 5.6: Hit pattern for the SSSSD in dashed blue with a fit according to Eq. (5.4). Histogram in red are data from a ggland simulation for comparison. Both histograms are normalized to 100 000 events. The lower part of the figure shows the ratio of hits between simulated and experimental data.

6 Analysis
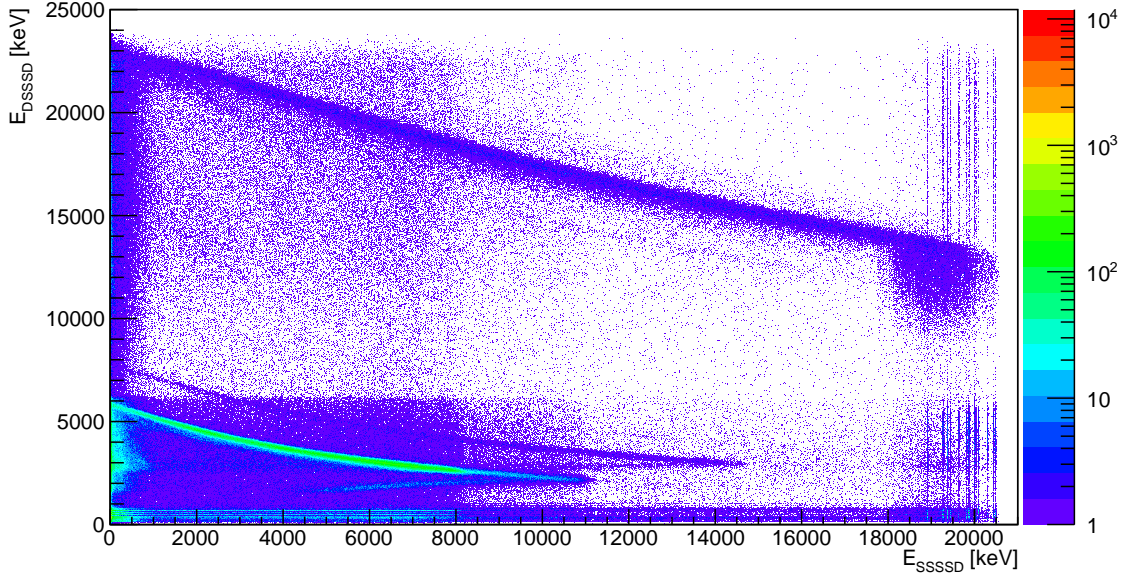
Figure 6.1: Calibrated but otherwise uncorrected plot of ΔE vs E for the telescope with the polyethylene target.

6.1 Energy matching

Once calibration parameters are extracted from the α source run, the UCESB unpacker was used to map both calibrated[1] and raw ^{21}Na+p data to ROOT-files. The calibrated data was used to match energy of the front and back side of the DSSSD. When a possible match was detected the energy was recalculated from the raw channel data using the gain and offset from the matrix in Eq. (5.2). If the energy was still considered as matching this value was saved and written into a new branch.

For obvious reasons it is enough to use the energy value from one of the two sides of the detector, but information about which intersecting strip corresponds to this energy is crucial for the determination of the scattering angle. For events with a multiplicity

---

[1]UCESB provides calibrated data with gain and offset input strip by strip.
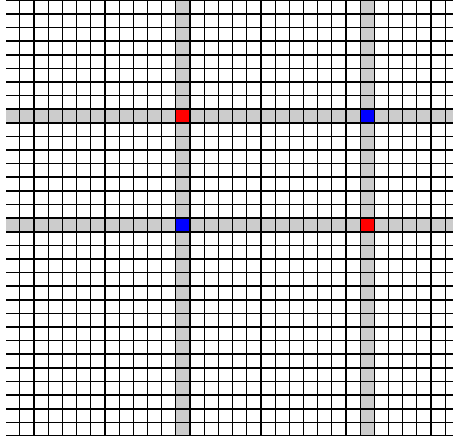
Figure 6.2: Two strips firing on both sides of the ΔE detector during the same event. The red and blue squares illustrate the ambiguity of the actual combination without energy matching of the front and the back side.

higher than 1, one must be able to assign the deposited energy to the corresponding pixel.

Another possibility is to have the energy of a particle shared between two adjacent strips. But high overall multiplicity in the DSSSD made it difficult to distinguish a potential energy split from noise in the neighboring strip.[2] Because of this only "clean" hits, where there were no adjacent strip firing during the same event, were accepted to avoid including spurious energies.

From Eq. (2.13) the excitation energy of the compound system depends on θ_{lab} but since it is impossible to know exactly where in the pixel the particle actually hits; the best one can do is to randomize its position within the pixel boundaries.

It would also be desirable to use a time gate at the both sides of the DSSSD but due to problems with the read-out from the backside[3] this could not be implemented.

6.2 ΔE-E alignment

To obtain the total energy of a impinging particle in the detector telescope one has to sum up the energy of both the ΔE and E detector. To assign the correct energy that the particle deposits in each detector the trajectory has to be considered, this was done by requiring alignment of the strips of the both detectors. Figure 6.3 shows the strip number of the ΔE versus E. This figure reveals that strip 1 of the front side of the DSSSD was approximately in horizontal alignment with strip 32 of the SSSSD. This was used to suppress unrealistic particle trajectories.

---

[2]If two adjacent strips are firing during the same event one would like to sum up the energies of these two and consider that as the actual energy deposited by the particle.

[3]Many multiplicity 1 events within the whole energy range were assigned T=0 from the back side.
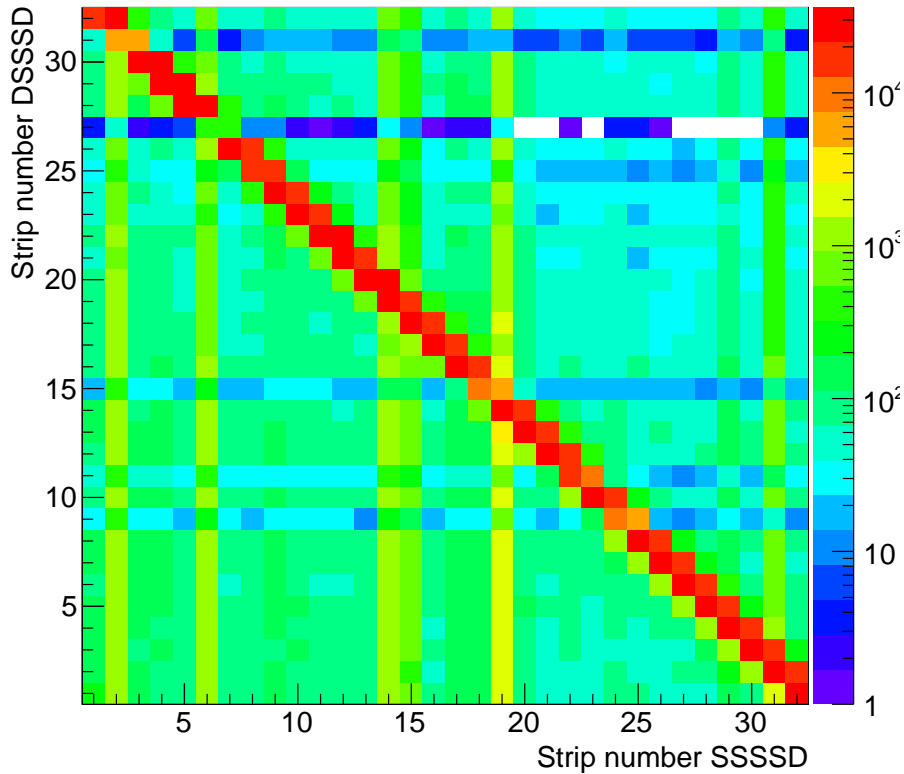
Figure 6.3: Alignment of horizontal strips in the DSSSD and the SSSSD using events with multiplicity 1.

Due to the lack of a time calibration only a rough estimate for the time of flight between the two detectors was made. In Figure 6.4 the time difference[4] between the SSSSD and the DSSSD versus the total proton energy can be seen. The rather broad spread of the band around ΔT≈0 is a consequence of the superposition of all alignment possibilities between the detectors. The small band at ΔT≈-1000 appears since all energies ≲800 keV were assigned T=0. The time of flight between the DSSSD and the SSSSD might still be able to provide a condition for reducing some of the background in the proton spectrum.

---

[4]The time difference is masured in channels.
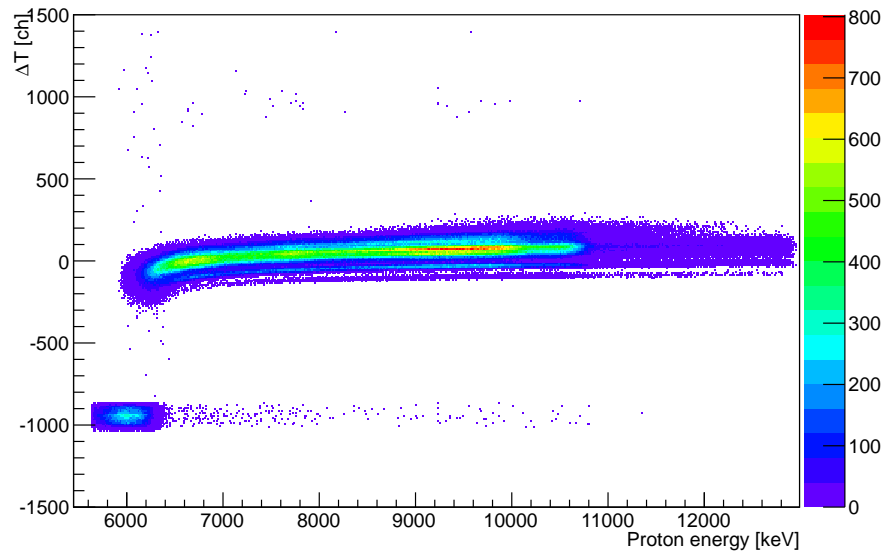
Figure 6.4: Time of flight between the ΔE and E detector versus the total proton energy.
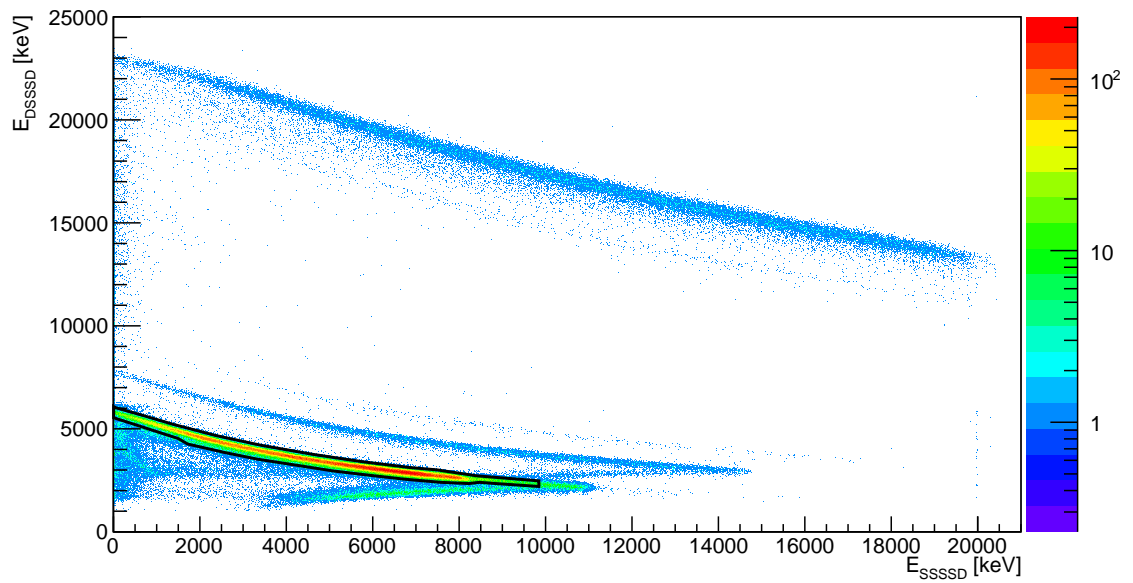
Figure 6.5: Energy measured in the ΔE versus the E detector after energy matching and strip alignment with a proton cut.
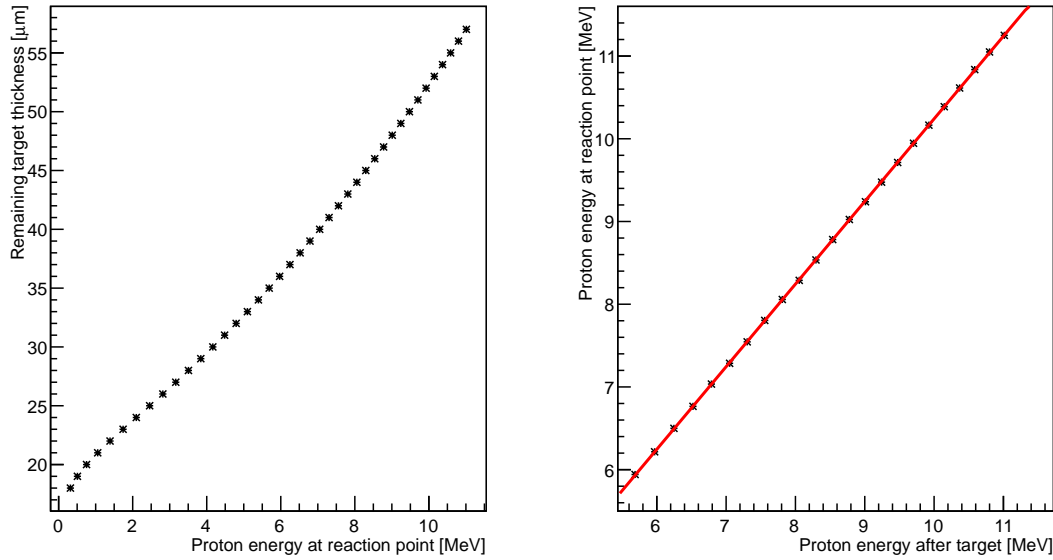
Figure 6.6: To the left: the remaining distance to travel in the target for the scattered protons versus their energy. To the right: the remaining proton energy after passing the target versus the energy at the the location of the decay. The mean energy loss is about 245 keV in the lab or ≈ 60 keV in the center of mass frame.

6.3 Energy losses

In addition to the energy loss in the dead layers of the silicon detectors also losses in the polyethylene target need to be taken into account. From the energy and the angle of the scattered protons it is possible to find the energy required for the ^{21}Na projectile necessary for this, Eq. (2.12). The remaining distance in the target for the proton to travel depending on energy is visualized in Figure 6.6 and was found by iterating the remaining energy of ^{21}Na as it travels through the target.

Since scattering angles around $10°$ imply an effective increase of the target thickness by $\approx 2\%$ the corresponding energy loss difference for protons in the range 6-11 MeV is around 5 keV[5] in the laboratory system. The approximately same energy loss for all these proton energies is a consequence of the distance travelled in the target by the ^{21}Na, giving rise to different proton energies[6], Eq. (2.12).

The proton energy in the center of mass system was calculated using the elastic

---

[5]Due to these small energy differences all losses in the target were calculated at $\theta_{lab} = 0°$ for simplicity.

[6]Assuming a lifetime of the resonance of 10^{-20}s, would at the speed of light travel for about 10^{-10}m in the target so the compound nucleus energy loss in the target is totally negligible.

scattering kinematics of ^{21}Na+p and the compound nucleus excitation energies from Eq. (2.13), are given by

$$E_X = S_p + \frac{(m_{Na} + m_p)T_p}{4m_{Na}\cos^2(\theta_p)} \tag{6.1}$$

where T_p is the proton lab energy, θ_p the scattering angle in the lab system and m_{Na}, m_p the mass of ^{21}Na and the proton respectively. The proton separation energy, $S_p = (m_{^{21}Na} + m_p - m_{^{22}Mg}) \approx 5504$ keV is based upon the masses [25].

6.4 Background subtraction

Not all of the detected protons stem from ^{21}Na+p reactions. Since the polyethylene target contains also carbon, the proton spectrum is a superposition of the desired protons from ^{21}Na+p and of protons from ^{21}Na+C reactions [26]. To be able to subtract the unwanted protons separate runs with a pure carbon target were made. All proton events from these were treated as if they were originating from resonant proton scattering reactions with ^{21}Na. This is certainly the wrong kinematics for protons from ^{21}Na+C reactions but it allows of subtraction of the carbon part from from the $(CH_2)_n$ spectrum.

Figure 6.7 shows protons from runs with both the $(CH_2)_n$ and the carbon target calculated as excitation energies, Eq. (2.13), of ^{22}Mg. From Figure 6.7 all protons above $E \approx 8450$ keV seems to emerge from reactions with the carbon in the polyethylene target. The carbon data is in Figure 6.7 scaled to fit this tail.
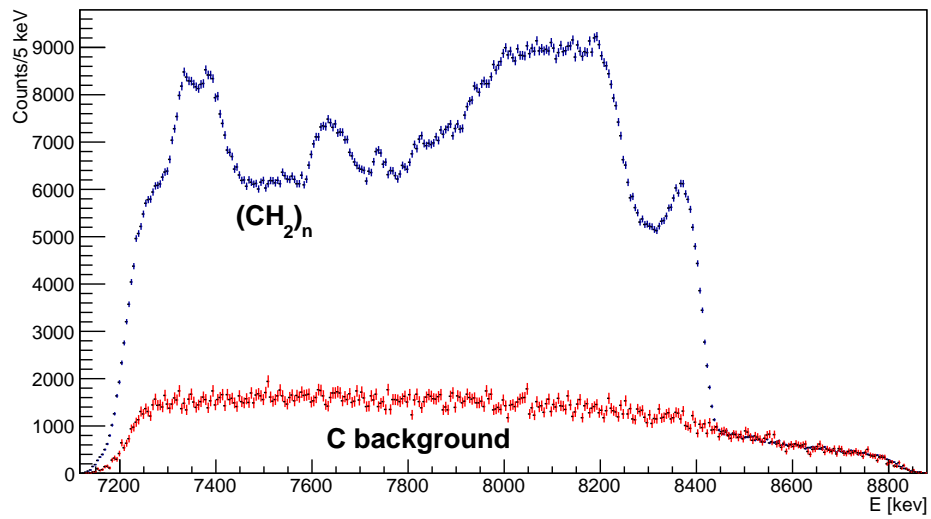
Figure 6.7: Proton spectra from the polyethylene and carbon runs, both calculated as ^{22}Mg excitation energies, Eq. (7.1).
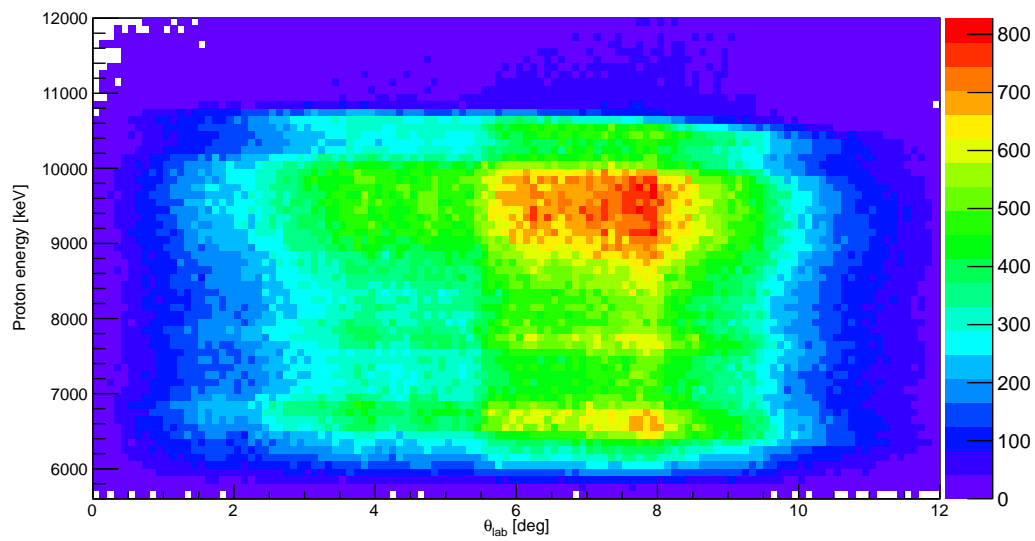
Figure 6.8: Proton scattering angle versus total kinetic energy in the detectors. The average scattering angle was $\theta_{lab} \approx 6° \Leftrightarrow \theta_{cm} \approx 168°$.

7 Results

With the background contribution from carbon subtracted all the remaining protons are expected to originate from the resonant proton scattering reaction ^{21}Na(p,p)^{21}Na[1].

Since the resonances in ^{22}Mg are short lived there are energy uncertainties and thereby a corresponding width of the energy peaks, typically Breit-Wigner distributed. This distribution should be convoluted with the Gaussian response function of the detectors. Such a convolution could not be fitted to the spectrum, instead a zeroth order approximation with pure Gaussians was used. No information about the width of the states can be achieved from this but the fit acts more as a smoothening of the spectrum. The energies of the excited states of ^{22}Mg, though, should still be accurately given by the location of the peaks.

To be able to proceed further an R-matrix analysis fit to the differential cross section data is probably the best way to deduce the width, spin and parity of the states.

The pure ^{21}Na+p spectrum with a Gaussian fit[2] is presented in Figure 7.1 and all energies obtained from this is given in Tab. 7.1, values reported from previous experiments are also listed for comparison.

Since it was not possible to calculate the width of the states from the fit of Gaussians, the energies had to be compared with a pure proton spectrum, Ref. [27], and then matched with the values reported by He *et al.* [20] from R-matrix analysis.

The most prominent peaks not listed in Ref. [20] are the ones located at 7.363 MeV, just above 7.328 (7.27) MeV, and 7.745 close to 7.647 (7.59) MeV. There is also one possibly new state above the the α threshold, between 8.209 (8.18) MeV and 8.385 (8.31) MeV, at 8.328 MeV, although that peak is not very strong. The values in parenthesis are the latest available ones, obtained by He *et al.* [20].

To approximate the systematic errors of the data error propagation from the linear fits obtained by the calibration has been used. With G representing the gain factor and O the offset, the error in the energy, δE, for each detector was estimated, Ref. [9], as

$$\delta E \approx \pm\sqrt{\delta E_G^2 + \delta E_O^2 + 2\mathrm{cov}(G,O)}$$

The uncertainties of the two detectors were considered to be uncorrelated and the total systematic error was approximately 24 keV for 12 MeV protons and 20 keV at 6.5 MeV protons in the lab. The corresponding error in the center of mass system was then between 5 and 6 keV over the whole resonant proton energy range.

---

[1] Any contribution from the inelastic, ^{21}Na(p,p')^{21}Na reaction, is not considered in here.
[2] The $\chi^2/d.o.f$ of the fit is 329/221.

In the spectrum, Figure 7.1, and Tab. 7.1 both systematic and fitted errors are included.

7.1 Discussion

The energies from this analysis, Tab. 7.1, are about 50 keV higher than those reported in Ref. [19], which were extracted using an R-matrix analysis fit.

A comparison of the two ΔE vs E plots in Figure 3.1 and Figure 6.3 shows that the punch through of the SSSSD started about 1 MeV lower compared to the simulation for the detector setup. One possible explanation of this is that the SSSSD was not fully depleted during the experiment.
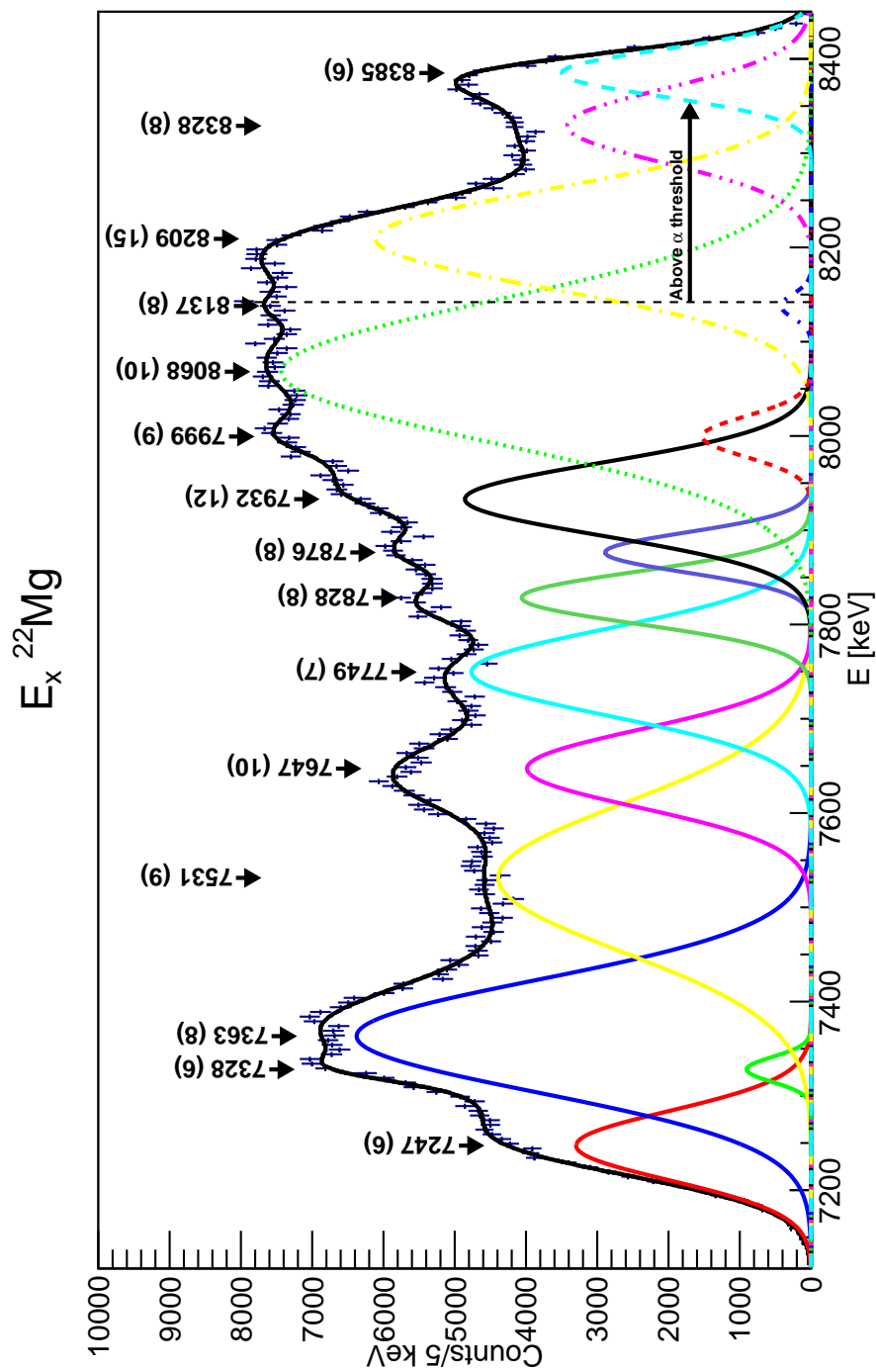
Figure 7.1: Spectrum of protons from resonant scattering of ^{21}Na+p as excitation energies in the ^{22}Mg nucleus. States above α threshold, indicated by the dashed line, are available for the ^{18}Ne(α,p)^{21}Na reaction. The average scattering angle was $\theta_{cm} \approx 168°$.

E_x	E_x [20]	E_x [21]	E_x [22]	E_x [23]	E_x [24]
-	6.61 (15)	6.606 (9)	6.606 (11)	6.616 (4)	-
-	6.81 (15)	6.766 (12)	6.767 (20)	6.771 (5)	6.760 (90)
-	6.92 (15)	-	6.889 (10)	6.878 (9)	-
-	7.06 (16)	-	-	-	-
7.247 (6)	-	-	-	-	-
7.328 (6)	7.27 (16)	-	-	-	-
7.363 (8)	-	-	-	-	-
-	7.42 (17)	-	7.402 (13)	7.373 (9)	-
7.531 (9)	-	-	-	-	-
7.647 (10)	7.59 (17)	7.614 (9)	-	7.606 (11)	-
7.749 (7)	-	-	-	-	-
7.828 (8)	-	-	-	-	-
7.876 (8)	7.82 (18)	-	7.784 (18)	7.757 (11)	7.784 (90)
7.932 (12)	-	-	-	-	-
7.999 (9)	7.98 (19)	7.938 (9)	7.964 (16)	7.986 (16)	7.890 (100)
8.068 (10)	-	-	-	-	-
8.137 (8)	-	-	-	-	-
8.209 (15)	8.18 (19)	8.197 (10)	8.203 (23)	8.229 (20)	-
8.328 (8)	-	-	-	-	-
8.385 (6)	8.31 (20)	-	-	-	8.290 (40)
-	8.51 (20)	8.512 (10)	8.547 (18)	-	8.550 (90)
-	8.62 (21)	8.644 (18)	8.613 (20)	8.598 (20)	-

Table 7.1: Energies of excited states in ^{22}Mg. E_x was extracted from all 5.6 mg/cm^2 (CH$_2$)$_n$ data. The C-background was subtracted and a sum of Gaussians was fitted to the resonant proton spectrum. All energies are in MeV, and errors in keV.

Bibliography

[1] Rolfs, C.E, & Rodney, W.S. (1988) *Cauldrons in the Cosmos*. United States of America: The University of Chicago Press

[2] ggland, *command-line simulation wrapper.* `http://fy.chalmers.se/~f96hajo/ggland/index.html` (2013-04-05)

[3] Geant4, *A toolkit for the simulation of the passage of particles through matter.* `http://geant4.cern.ch` (2013-04-05)

[4] The Isolde Facility. `http://ab-dep-op-iso.web.cern.ch/ab-dep-op-iso/HTML/hall_overview.htm` (2013-04-01)

[5] ROOT, *A Data Analysis Framework.* `http://root.cern.ch/drupal/` (2013-04-04)

[6] National Nuclear Data Center, *Chart of Nuclides.* `http://www.nndc.bnl.gov/chart/` (2012-09-12)

[7] CERN Hadron Linacs `http://linac2.home.cern.ch/linac2/` (2013-04-10)

[8] Ziegler, J.F., *SRIM The Stopping and Range of Ions in Matter.* `http://www.srim.org` (2012-09-14)

[9] Leo, W.R. (1994) *Techniques for nuclear and particle physics experiments*. Germany: Springer-Verlag Berlin Heidelberg

[10] Johansson, H. (2010) *Hunting tools beyond the drip lines*. Göteborg: Chalmers Reproservice

[11] Tengboen, E. (2009) *Transfer reactions in inverse kinematics at CERN-ISOLDE*. Göteborg: Chalmers Reproservice

[12] Krane, K.S. (1988) *Introductory nuclear physics*. 2nd ed. United States of America: John Wiley & Sons Inc

[13] Axelsson, L. (1999): *Exotic Nuclei - experimental studies of nuclear structure*. Göteborg: Chalmers Reproservice.

[14] Wiescher, M. et al (1999) Break-out reactions from the CNO cycles. *Journal of Physics G: Nuclear and Particle Physics 25(6)*, 133-161

[15] Bishop, S. et al (2003) ^{21}Na(p,γ)^{22}Mg reaction and oxygen-neon novae. *Physical Review Letters 90(16)*, 1-4

[16] Sachs M.W. et al (1966) Heavy ion reaction product identification by measurement of dE/dx and E. *Nuclear Instruments and Methods 41*, 213-225

[17] Ruiz, C. et al (2005) Multichannel R-matrix analysis of elastic and inelastic resonances in the ^{21}Na+p compound system. *Physical Review C 71*, 1-15

[18] Logbook for IS512, CERN-Isolde (2012) `http://www.miniball.york.ac.uk/mblog/mb/12941`

[19] He, J.J. et al (2008) A study of the proton resonant property in ^{22}Mg by elastic scattering of ^{21}Na+p and its astrophysical implication in the ^{18}Ne(α,p)^{21}Na reaction rate. *The European Physical Journal A 36*, 1-5,

[20] He, J.J. et al (2009) Investigation of excited states in ^{22}Mg via elastic resonant scattering of ^{21}Na+p and its atrophysical implications. *Physical Review C 80*, 1-5

[21] Berg, G.P.A et al (2003) Resonance States in ^{22}Mg for Reaction Rates in the rp-Process. *Nuclear Physics A 718*, 608-610

[22] Chen, A.A. et al (2001) Structure of ^{22}Mg and its implications for explosive nucleosynthesis. *Physical Review C 63*, 1-11

[23] Caggiano, J.A. et al (2002) Excitation energies in ^{22}Mg from the ^{25}Mg(^{3}He,^{6}He)^{22}Mg reaction. *Physical Review C 66*,1-5

[24] Alford, W.P. et al (1986) Structure of ^{22}Mg, ^{26}Si, ^{34}Ar and ^{38}Ca via the (^{3}He,n) reaction. *Nuclear Physics A 457*, 317-336

[25] Audi, G. et al (2012) The NUBASE2012 evaluation of nuclear properties. *Chinese Physics C 36(12)*, 1157–1286

[26] National Nuclear Data Center, *Q-value calculator.* `http://www.nndc.bnl.gov/qcalc/` (2013-02-21)

[27] He, J.J. et al (2004) Study of Proton Resonant States in ^{22}Mg using a Radioactive Beam of ^{21}Na. *CNS Annual Report 2004*, 1-2

A

A.1 Data files

The following data files were used:

DSSSD calibration: is512_run00180125.lmd - is512_run00180130.lmd

SSSSD calibration: source27Jul-7.lmd

Beam position: is512_run00090066.lmd - is512_run00090067.lmd

^{21}**Na+(CH$_2$)$_n$:** is512_run00090016.lmd - is512_run00090064.lmd (run00090046 excluded).

^{21}**Na+C:** is512_run00100087.lmd - is512_run001000103.lmd

A.2 Figures
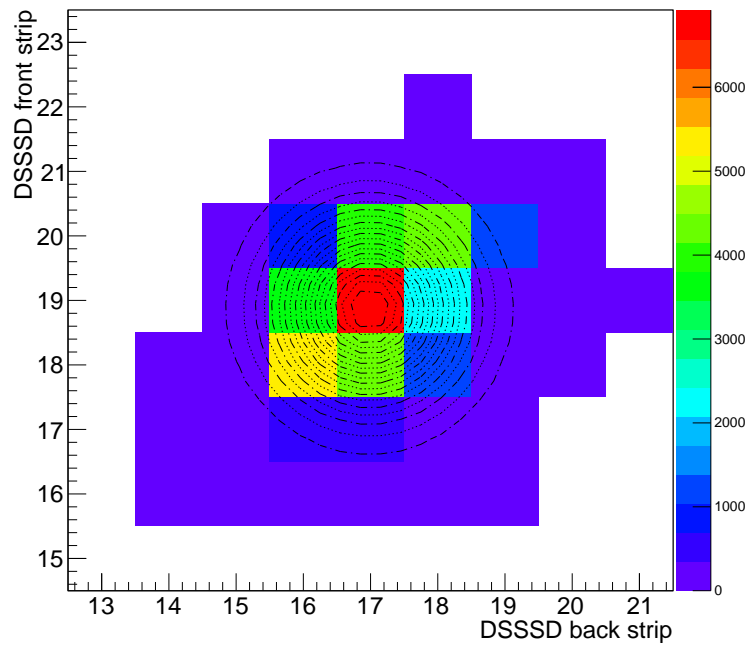
Figure A.1: Run for determining the beam position relative the detector.
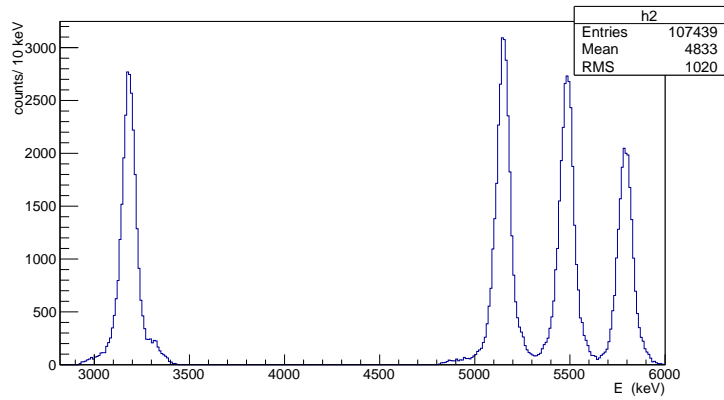
Figure A.2: Calibrated α spectrum of the SSSSD.
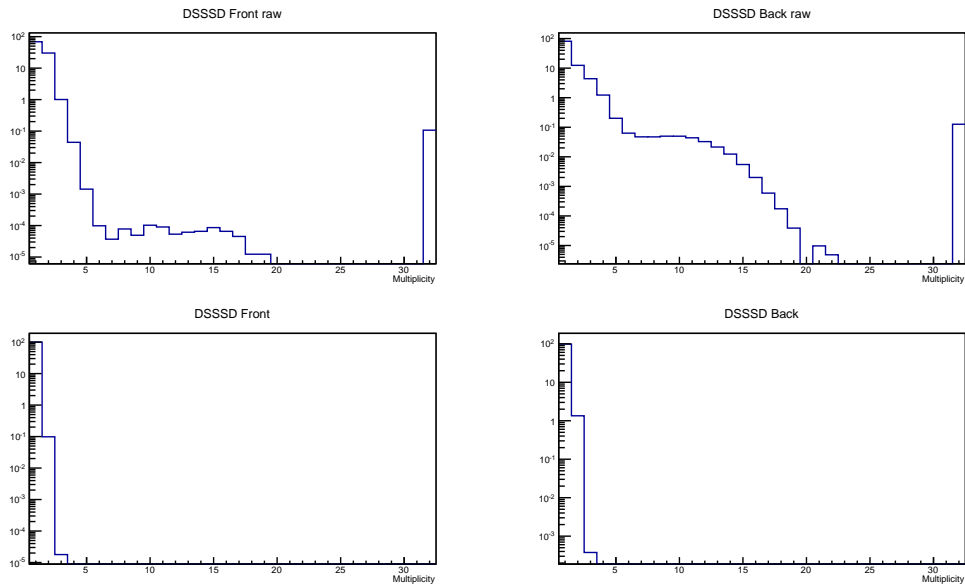
Figure A.3: The multiplicity of the calibration data. The upper two shows the multiplicity from the raw data and the lower two the multiplicity after an energy gate has been applied. The high multiplicity gave rise to a spurious hit pattern.
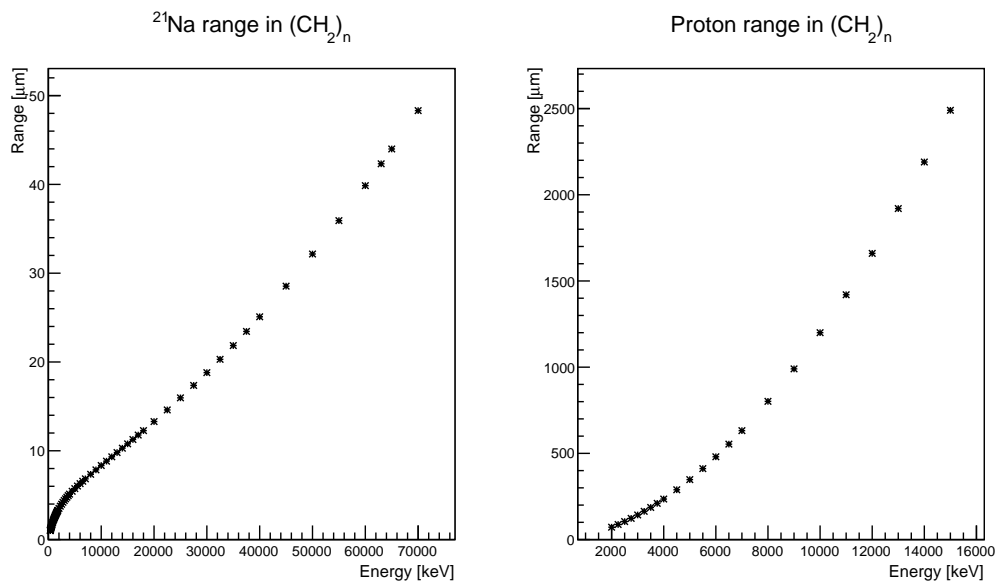
Figure A.4: The range of ^{21}Na and protons in the polyethylene target calculated by SRIM.
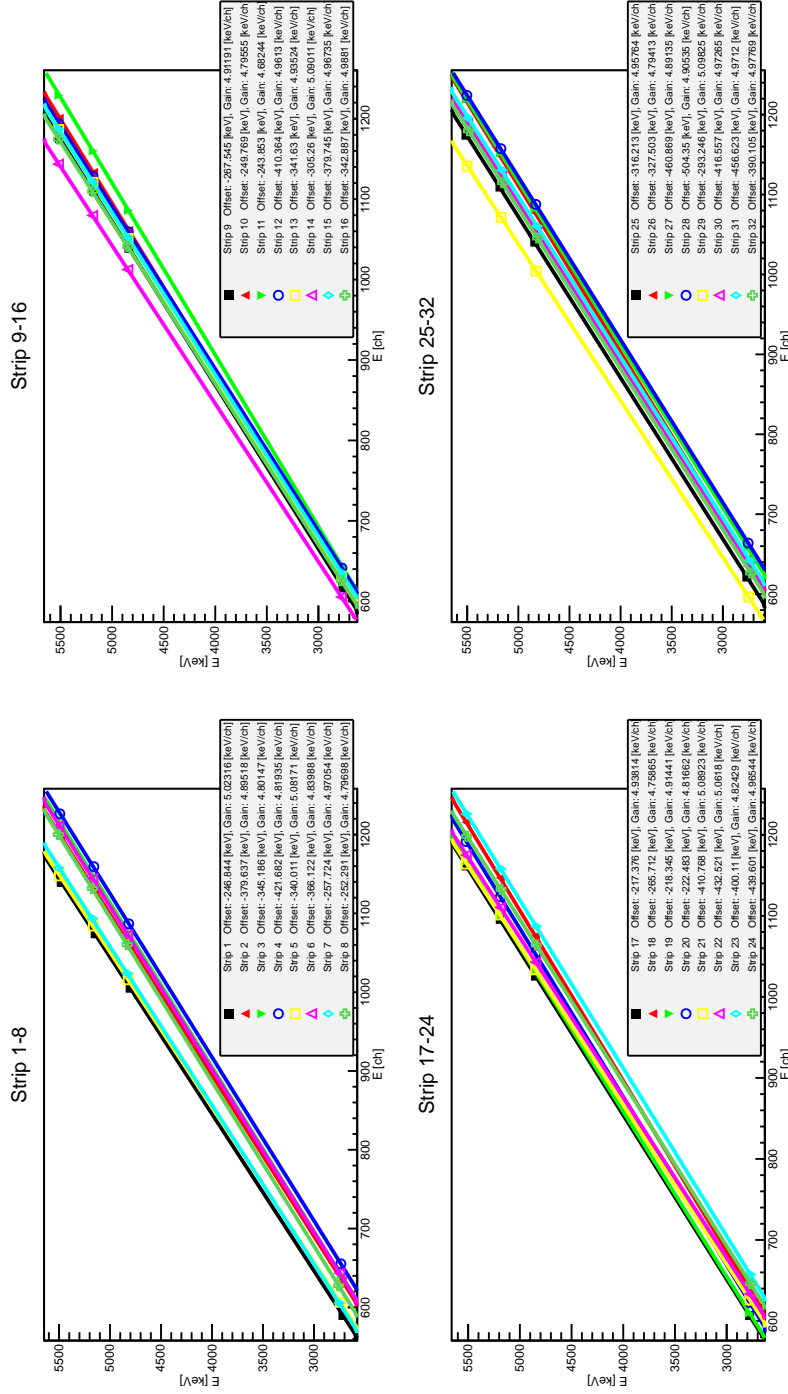
Figure A.5: Linear fits for all 32 strips of the SSSSD according to Eq. (5.5). Similar fits are made for the DSSSD but then for each pixel instead of for each strip yielding $32 \cdot 32 \cdot 2$ linear fits.